Progress in Quantum Electronics 59 (2018) 1–18

Contents lists available at ScienceDirect

Progress in Quantum Electronics

journal homepage: www.elsevier.com/locate/pqe

Review

Nanolasers: Second-order intensity correlation, direct modulation and electromagnetic isolation in array architectures

Si Hui Pan [a], Suruj S. Deka [b], Abdelkrim El Amili [b], Qing Gu [c], Yeshaiahu Fainman [b,*]

[a] Department of Physics and the Department of Electrical and Computer Engineering, University of California at San Diego, La Jolla, CA, 92093, USA
[b] Department of Electrical and Computer Engineering, University of California at San Diego, La Jolla, CA, 92093, USA
[c] Department of Electrical Engineering, University of Texas at Dallas, Richardson, TX, 75080, USA

ARTICLE INFO

Keywords:
Nanolaser
Second-order intensity correlation
Direct modulation
Coupled resonators
Tunable nanolasers
Semiconductor lasers
Nanoresonators
Nanostructures

ABSTRACT

Ideal integrated light emitters for optical interconnects should be compact in size, high in modulation bandwidth, efficient in energy consumption and tunable in frequency. Nanolasers are excellent candidates for such an application. In this article, we review and offer further in-depth analyses in three key aspects of recent nanolaser research, including second order intensity correlation, $g^2(\tau)$, characterizations, direct modulation and electromagnetic isolation in a dual nanolaser system. For coherence characterization, we review a technique exploiting not only the photon bunching peak, but also the $g^2(\tau)$ pulse width to determine the spontaneous emission (SE), amplified SE and lasing regimes of a nanolaser with a high SE factor, β. We show that this technique is applicable for lasers with β's ranging from 10^{-5} to unity. Additionally, we demonstrate the first direct current modulation of an electrically pumped metallo-dielectric nanolaser (MDNL) at 30 MHz. Considering the viability of nanolasers for dense integration, we then review the electromagnetic coupling between two closely spaced MDNLs and identify two practical methods to eliminate such coupling. Lastly, we review the state-of-the-art development in and offer future perspectives on three other important areas of nanolaser research – integration with silicon photonics, wide-range frequency tuning and dual nanolaser dynamics.

1. Introduction

NANOLASERS are ultra-compact coherent light emitters, which can be densely integrated on-chip with potential applications ranging from high-speed optical computing [1] and sensing [2] to chemical detection [3–5] and nonlinear optical microscopy [6]. In particular, enabling ultrafast, energy-efficient all-optical or hybrid computing can reduce annual electricity consumption of large data centers by hundreds of terawatt-hours, which constitutes a significant portion of the global energy consumption [7–10]. Towards this end, in recent years, nanolaser research has shifted in direction from proof-of-concept demonstrations of novel nanoresonator architectures to the development and investigation of nanolasers with high spontaneous emission factors (β). High-β lasers can theoretically achieve ultra-low threshold energy since most of the spontaneous emission (SE) is funneled into the lasing mode [11]. Furthermore, applications centered on high-speed on-chip communication and computing demand research focused on nonlinear dynamical phenomena [12] [13], direct modulation [14–20] and array architectures [21]. In addition to the advantages from an application standpoint, the studies of nonlinear dynamics in nanolasers reveal interesting physics, such as dynamical hysteresis [12], spontaneous

* Corresponding author.
E-mail addresses: h0pan@ucsd.edu (S.H. Pan), sdeka@eng.ucsd.edu (S.S. Deka), aelamili@eng.ucsd.edu (A. El Amili), qing.gu@utdallas.edu (Q. Gu), fainman@ece.ucsd.edu, fainman@eng.ucsd.edu (Y. Fainman).

https://doi.org/10.1016/j.pquantelec.2018.05.001

Available online 31 May 2018

symmetry breaking [13], asymmetric mode scattering [22] and super-thermal photon statistics [23], [24]. Therefore, nanolasers also provide excellent miniaturized platforms to explore fundamental physics in the field of nonlinear dynamics.

In this article, we aim to review some of the exciting results in the field of nanolaser from three different aspects, including second-order intensity correlation studies, direct modulation and coupled nanolasers. Regardless of whether the focus is on practical applications or fundamental physics, the first step of any nanolaser-based research is to characterize the coherence and threshold properties of the nanodevices, since knowledge about their thresholds is often a prerequisite for any further study. While such characterizations are relatively trivial for macroscopic lasers with small β factors (i.e. $\beta \ll 1$), it becomes increasingly difficult for high-β nanolasers with β factors approaching unity. Therefore, we dedicate the next section of this article to review recent research efforts in overcoming this challenge. In the third section, we review research endeavors to directly modulate single, isolated nanolasers for optical signal processing. In the fourth section, we shift our focus to coupled nanolasers research, which provides a pivotal understanding of how nanolasers may behave in a densely packed, large-sized array. Finally, we will discuss the future perspectives of nanolasers research and summarize our discussion in section 5.

2. Coherence and threshold characterization of high-β nanolaser

The spontaneous emission factor is defined as the fraction of the spontaneous emission that's channeled into the lasing mode defined by

$$\beta = \frac{SE_{lasing}}{SE_{lasing} + SE_{nonlasing\ modes} + SE_{free\ space\ continuum}}, \tag{1}$$

where SE_{lasing}, $SE_{nonlasing\ modes}$ and $SE_{free\ space\ continuum}$ represent the spontaneous emission into the lasing mode, other nonlasing cavity modes and the free space continuum, respectively. A commercially available laser diode typically has a β factor on the order of 10^{-3} or lower [25]. On the other hand, high-β nanolasers discussed in this article have β factors ranging from 0.1 to unity.

2.1. Motivation

Theoretically, a high-β nanolaser can lase at a threshold much lower than that of a laser with a small β factor since most of the

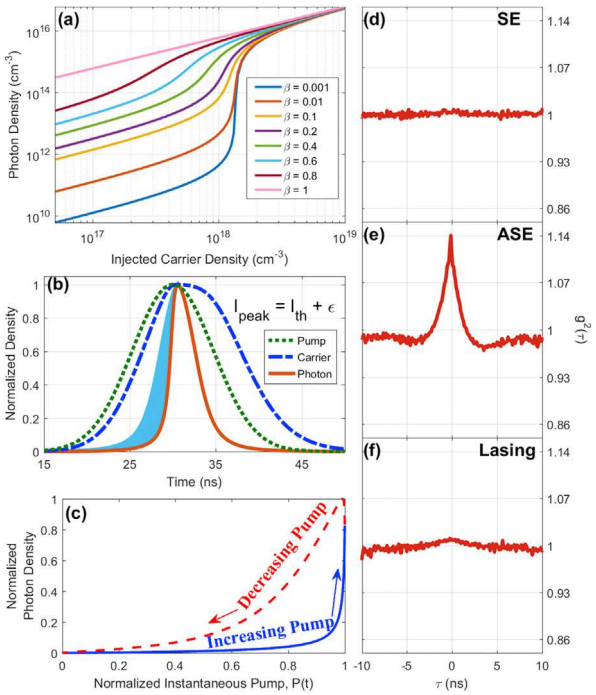

Fig. 1. (a): LL-curves simulated by solving the laser rate equations [equations (2) and (3)] at steady state (i.e. setting the left sides of equations equal to zero) for different values of β. The kink in the LL-curve, conventionally used to define the lasing threshold, vanishes as β approaches unity. (b): The normalized output photon pulse (solid orange) of the nanolaser simulated with equations (2) and (3) with parameters shown in Table 1. The asymmetry observed in the emitted photon pulse is due to the delayed threshold phenomenon. The pump pulse (dotted green) and the carrier density (dashed blue) are also shown for reference (reprinted from Ref. [12]). (c): A dynamic hysteresis loop is obtained by plotting the output photon density in (d) as a function of the instantaneous pump intensity. (d)–(f): Normalized $g^2(\tau)$ in the SE (d), ASE (e) and lasing (f) regimes obtained experimentally. The photon bunching peak visible in the ASE regime in (e) vanishes in the SE and lasing regimes due to Poissonian statistics and the detector averaging effect, respectively. The $g^2(0)$'s in (d), (e), (f) correspond to the data points labeled as I, II, III in Fig. 2(b). (For interpretation of the references to colour in this figure legend, the reader is referred to the Web version of this article.)

spontaneous emission is funneled into the lasing mode for the former [11]. Therefore, the energy efficiency of a high-β nanolaser can be significantly higher compared to nanolasers of a similar design, but with comparatively smaller β factors. In addition, a high-β nanolaser, in general, has an extremely small mode volume causing the number of optical modes supported by the cavity to be significantly reduced. Since Purcell effect can be strongly enhanced in nanocavities with ultra-small mode volumes [26] [27], leading to increased spontaneous emission rates, high-β nanolasers can theoretically be modulated at ultra-high speeds.

Unsurprisingly, a nanolaser with a unity-β factor is the most desirable as it will theoretically have the lowest threshold and the highest modulation bandwidth. We can generate the light-in versus light-out curves (LL-curves) of lasers with different β factors by numerically solving the laser rate equations [28] at steady state [Fig. 1(a)]. It is well known that as β approaches unity, the kink in the LL-curve, conventionally used to define the lasing threshold, diminishes and altogether disappears when $\beta = 1$ [Fig. 1(a)]. Therefore, measurement of a kinkless LL-curve is one experimental method to demonstrate unity-β lasing. However, while unity-β lasing can lead to a kinkless LL-curve, the reverse is not always true. That is, a kinkless LL-curve by itself does not necessarily indicate unity-β lasing. The SE (i.e. far below threshold regime indicated by the kink) or lasing (i.e. far above threshold) sections of the LL-curves with any arbitrary β values [Fig. 1(a)] are also kinkless. Hence, a kinkless LL-curve can also be obtained experimentally due to either insufficient input intensity to reach the lasing threshold, or, in the more optimistic case, a lasing threshold too low to be detected. Furthermore, a kinkless LL-curve does not offer information about the lasing threshold, which is an indispensable parameter to know if practical applications such as those involving direct modulation are to be realized.

Compared to the LL-curve method, measuring the second-order intensity correlation function of a nanolaser's output, $g^2(\tau) = \frac{\langle I(t)I(t+\tau)\rangle}{\langle I(t)\rangle\langle I(t+\tau)\rangle}$, with a Hanbury Brown-Twiss (HBT) interferometer is a more definitive technique to confirm lasing and to characterize the threshold of a unity-β nanolaser. It is well known that an incoherent source exhibits intensity fluctuations leading to a photon bunching peak in $g^2(\tau)$ near zero delay (i.e. $|\tau| \approx 0$) such that $g^2(0) > 1$. Specifically, $g^2(0)$ approaches a value of two for an ideal thermal source such as a perfect black body emitter. On the other hand, a coherent emitter such as a laser above threshold follows Poissonian statistics such that $g^2(0) = 1$ [29].

2.2. Review of $g^2(\tau)$ studies of nanolasers

2.2.1. Photon bunching peak or $g^2(0)$

From a theoretical perspective, Chow et al. presented a rigorous investigation of the intensity, coherence time and $g^2(0)$ as functions of pump current for nanolasers with β's of 0.01 and unity [30]. Their theoretical model employed full quantum-optical descriptions of the active medium, comprised of quantum dots (QDs) embedded in quantum wells, and the radiation field while approximating the light-matter interaction up to the second order. By comparing the results of nanolasers with β's of 0.01 and unity, Chow et al. concluded that the transition from SE to lasing existed even for a unity-β nanolaser. Although such a transition was difficult to identify from a nearly linear LL-curve for a unity-β nanolaser, it could be easily discerned by inspecting both the $g^2(0)$, which transitioned from super-Poissonian [i.e. $g^2(0) > 1$] to Poisson [i.e. $g^2(0) = 1$] statistics with an increasing pump current, as well as the coherence time, which increased slowly in the SE regime but rapidly in the lasing regime as pump current increased. Curiously, the comprehensive model also predicted that non-classical [i.e. $g^2(0) < 1$] light emission could be generated as the number of QD is reduced to ten and below for a lasing cavity with β equal to 0.01 and photon lifetime of 20 ps?

From an experimental standpoint, Strauf et al. [31] and Choi et al. [32] first applied the HBT technique to study the coherence transitions of optically pumped PhC nanolasers operating at 4 K. While Strauf et al. measured $g^2(0)$ versus pump power for only one PhC nanolaser to demonstrate its lasing characteristics, Choi et al. conducted more in-depth analyses with a family of PhC nanolasers. They demonstrated the convergence to Poissonian statistics, i.e. $g^2(0) = 1$, for three PhC nanolasers with estimated β factors equal to 0.19, 0.44 and 0.69, respectively. In addition, Choi *el al.* discovered that high-β nanolasers exhibit a soft-turn-on such that the amplified spontaneous emission (ASE) regime spans a wide range of input pump intensities. The soft-turn-on behaviors are observable in both the LL-curves and the $g^2(0)$ versus pump curves. They further show that the lasing transition or the ASE regime becomes broader as β increases. Following Choi, Hostein et al. also exploited the HBT technique and measured $g^2(0)$ as a function of pump intensity to confirm lasing in a PhC nanolaser with an estimated β factor greater than 0.1 [33]. While Hostein's nanolaser has a smaller β factor than those studied by Choi, this device operates at room temperature under pulsed optical excitation and emits at the telecom wavelength around 1535 nm, which is more suitable for practical applications. A room-temperature PhC nanolaser with a β factor as high as 0.85 was reported by Prieto *el al.* [34]. However, the authors did not perform any $g^2(\tau)$ measurements with their device.

While PhC nanolasers can exhibit ultra-small mode volumes, their physical footprints are on the order of at least tens of microns due to the need of many dielectric lattice periods to achieve high quality factor, Q, and good optical confinement. The search for a nanolaser with sub-wavelength dimensions in terms of not only mode volume, but also physical size (i.e. footprint) leads to the development of SPASERs [35–42] and metal-clad photonic-mode nanolasers (MCPMNL) [43–47]. Noginov et al. demonstrated the first SPASER based on nanoparticles with gold cores and dye-doped silica shells in 2009 [35]. However, the authors did not conduct any $g^2(\tau)$ measurements. Furthermore, with only five data points in the LL-curve, the β factor could not be retrieved. In the same month as Noginov et al.'s publication, a unity-β SPASER based on a cadmium sulfide nanowire operating at cryogenic temperature below 10 K was reported by Oulton et al. [37]. However, no $g^2(\tau)$ measurement was reported either in this publication. It was not until 2012 that the first SPASER demonstration accompanied by $g^2(\tau)$ measurements was conducted by Lu et al. [40]. Their SPASER consisted of an epitaxially grown silver film, a 5-nm silicon dioxide layer and an epitaxially grown InGaN nanorod. With an estimated β factor of 0.73, this nanolaser operated with continuous wave (CW) optical pumping at 8 K. While these authors did not conduct detailed studies on the coherence transition by plotting $g^2(0)$ as a function of pump intensity, they did conduct HBT measurements at one pump intensity below threshold

and another one above threshold. The below-threshold $g^2(\tau)$ exhibited a photon bunching peak, which is suppressed at high pump intensity, therefore, confirming lasing in this nanorod SPASER.

MCPMNLs represent another promising architecture with sub-wavelength mode volumes as well as physical dimensions. A unity-β MCPMNL with a coaxial resonator design was reported by Khajavikhan et al. in 2012 [45]. Detailed $g^2(\tau)$ studies on high-β MCPMNLs have been carried out recently, which unambiguously confirm their lasing characteristics [12], [48]. For example, Fig. 1(b)–(f) and Fig. 2 show the results of Pan et al. who measured the $g^2(\tau)$ function of a room-temperature metallo-dielectric nanolaser under nanosecond-optical-pulse pumping [12]. The normalized $g^2(\tau)$ function in the SE, ASE and lasing regimes is shown in Fig. 1(d)–(f). Photon bunching is evident in the ASE regime. The height of the photon bunching peak, i.e. $g^2(0)$, was plotted as a function of pump intensity in Fig. 2(b). The photon bunching peak was found to be suppressed and $g^2(0)$ approaches unity at high pump intensity due to lasing. In contrast to theoretical expectations, a photon bunching peak was not observed in the SE regime. The authors explained that this observation was due to the coherence time becoming shorter than the detector resolution in the SE regime such that the $g^2(0)$ peak is washed out by detector averaging effect. Additionally, due to the relatively large β ($\approx$0.25) of the device, both the LL-curve [Fig. 2(a)] and $g^2(0)$ curve [Fig. 2(b)] exhibit a soft-turn-on behavior. These results are consistent with findings presented by Choi et al. with PhC nanolasers [32].

2.2.2. *Dependency of $g^2(\tau)$ pulse width on light emission statistics*

Interestingly, Pan et al. demonstrated that the photon bunching peak, i.e. $g^2(0)$, is not the only parameter to characterize lasing or to identify the threshold. In fact, the width of the $g^2(\tau)$ pulses can also be exploited to identify the SE, ASE and lasing regimes of a room-temperature metallo-dielectric nanolaser under nanosecond-optical-pulse pumping. Note that the width of concern here is not the width of the photon bunching peak such as that shown in Fig. 1(e), but rather the width of the auto- (i.e. $\tau = 0$) or cross-correlation ($\tau \neq 0$) of the optical pulses emitted by the nanolaser.

As shown in Fig. 2(c), the $g^2(\tau)$ pulses are much broader in the SE regime than they are in the ASE and lasing regimes. Furthermore, the $g^2(\tau)$ pulse width shrinks with increasing pump intensity in the SE regime, reaches a minimum in the ASE regime and broadens with increasing pump intensity in the lasing regime. The contrasting behavior of the $g^2(\tau)$ pulse width with respect to the pump intensity above and below threshold indicates that the emission statistics in the SE and lasing regimes are indeed very different despite the fact

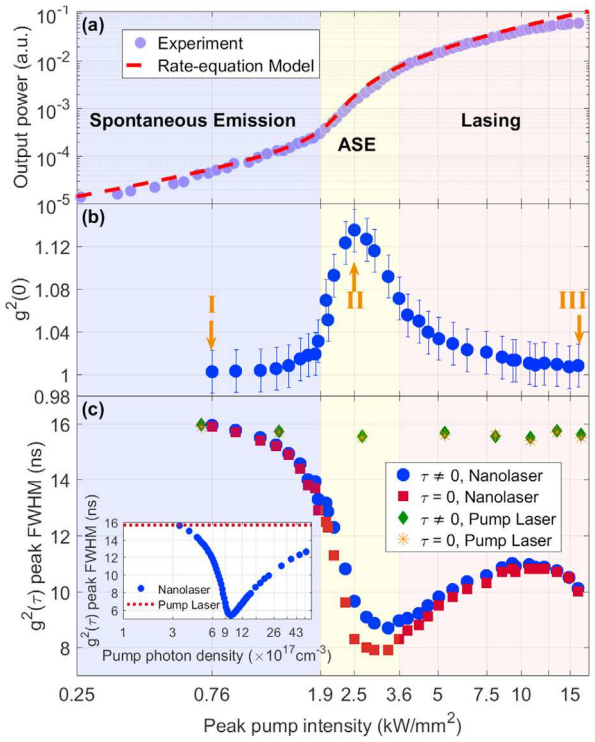

Fig. 2. (a) An experimental LL-curve of a metallo-dielectric nanolaser. The dashed red is generated by numerically solving equations (2) and (3) with $\beta = 0.25$. Other parameters used in these equations are defined and specified in Table 1. (b) An experimental $g^2(0)$ curve as a function of pump intensity. The normalized $g^2(\tau)$ corresponding to data points labeled I, II, III are shown in Fig. 1(d), (e), (f). Photon bunching is apparent in the ASE regime due to partially incoherent emission. It is suppressed in the lasing regime due to coherent emission and in the SE regime due to the detector averaging effect. (c) An experimental curve of $g^2(\tau)$ pulse width versus pump intensity curve. The pulse width is broad and shrinks with increasing pump intensity in the SE regime while it is relatively narrower and broadens as pump intensity increases in the lasing regime, indicating that the emission statistics are indeed very different in the two regimes even though $g^2(0)$ approaches unity in both cases. It also indicates that the $g^2(\tau)$ width can be used as a separate parameter to characterize the SE, ASE and lasing regimes of a laser. Inset: the simulated $g^2(\tau)$ width variation, which agrees well with the experimental observations, is generated by numerically solving the laser rate equations. (Reprinted from Ref. [12]). (For interpretation of the references to colour in this figure legend, the reader is referred to the Web version of this article.)

that $g^2(0)$ approaches unity in both regimes. These authors further recognized that the pulse shape variation is not due to photon bunching because the photon bunching peak arises on top of the zero-delay (i.e. $\tau = 0$) pulse only. However, both the zero-delay pulse and the non-zero-delay pulses show similar dependence on the pump intensity. To explain the pulse shape variations in the different operating regimes of the nanolaser, a rate-equation model was employed to examine the transient photon and carrier densities of the nanolaser under nanosecond pulse pumping. By solving the rate equations numerically, the simulated $g^2(\tau)$ pulse width variation as a function of injected carrier density [Fig. 2(c) inset] was shown to be consistent with experimental observations [12].

In addition, by examining the simulated output photon pulse of the nanolaser, Pan et al. discovered that the pulse becomes asymmetrical above threshold [Fig. 1(b)] due to an intensity jump occurring on the left side of the pulse. They explained that such asymmetry originates from the delayed threshold phenomenon (DTP), a well-known effect observed in any dynamically driven nonlinear system such as a laser driven by a fast-varying pump current [49–53]. Fig. 1(c) is obtained by plotting the right- and left-hand side of the photon pulse in Fig. 1(b) simultaneously as a function of the normalized instantaneous pump power, $P(t)/P_{max}$. A hysteresis loop is manifested in Fig. 1(c), which is conventionally referred to as the dynamical hysteresis (DH) loop in the literature [49–53]. Since the DTP induced DH can be observed only when the pump is swept across threshold [49–53], as the peak pump intensity increases, the pump intensity crosses threshold at an earlier time and the intensity jump in the output of the nanolaser also happens earlier, leading to broadening of the output photon pulse, which was observed experimentally. In summary, Pan et al. concluded that the above threshold broadening in the $g^2(\tau)$ pulse width was an indirect experimental observation of the DTP or DH, which served as an independent confirmation that lasing had occurred. They further recognize that the $g^2(\tau)$ pulse width can be used as a separate metric to characterize the SE, ASE and lasing regimes, as well as to estimate the threshold of a high-β nanolaser [12].

2.3. $g^2(\tau)$ pulse width versus β for MCPMNL

The technique of exploiting the $g^2(\tau)$ pulse width to characterize coherence and to estimate the lasing threshold can be applied to MCPMNL with any β values. We demonstrate this procedure by solving the coupled laser rate equations for $\beta = 10^{-5}$, 0.1, 0.25, 0.5, 0.7 and 1. The rate equations adopted for this simulation are shown in Eqs. (2) and (3) [12] [28], with the parameters defined and specified in Table 1.

$$\frac{dS}{dt} = \Gamma g_0 (N - N_0) S - \frac{S}{\tau_p} + \frac{\Gamma \beta N}{\tau_{rr}} \tag{2}$$

$$\frac{dN}{dt} = I_{peak} \exp\left[\frac{(t - t_0)^2}{\Delta^2}\right] - \frac{N}{\tau_{rr}} - \frac{N}{\tau_{nr}} - g_0 (N - N_0) S \tag{3}$$

By numerically solving Eqs. (2) and (3), the transient photon density representing a single emission pulse of the nanolaser can be simulated. The simulated emission pulses of nanolasers with β of 10^{-5} and unity are shown on the left side of Figs. 3 and 4, respectively. The corresponding autocorrelation functions, i.e. $g^2(\tau)$, of the emission pulses are shown on the right side of Figs. 3 and 4. Similar to the findings in Ref. 12, the output photon pulse is broadest far below threshold. The photon pulse width subsequently shrinks as the pump intensity increases. The minimum width is found slightly above threshold (i.e. $P = P_{th} + \varepsilon$), after which the pulse broadens as the pump intensity continues to increase. Comparison of results in Figs. 3 and 4 shows that both unity-β lasers and lasers with negligibly small β

Table 1
Descriptions and values of the symbols used in the rate-equation simulation.

Symbol	Description	Value
S	photon density	
N	carrier density	
P_{peak}	peak pump (injected) carrier density	
$FWHM$	full width at half maximum of optical pump pulse	
Δ	FWHM/$(2\sqrt{\ln 2})$	6.65 ns
t	time	0–80 ns
t_0	time when the Gaussian pump pulse reaches maximum	30 ns
Γ	energy confinement factor	0.6
G	linear gain coefficient	5×10^{-16} cm^2 [54]
n_g	group refractive index for InGaAsP	3.5 [19] [54] [55],
c	speed of light	3×10^8 m/s
v_g	group velocity	$v_g = c/n_g = 8.57$ cm/ns
g_0	$v_g \times G$	4.285×10^{-15} cm^3/ns
N_0	transparency carrier density	2×10^{18} cm^{-3} [19] [55],
Q	cavity quality factor	3474
β	spontaneous emission factor	10^{-5}, 0.1, 0.25, 0.5, 0.7, 1
λ	emission wavelength	1550 nm
τ_p	photon lifetime	$(Q\lambda n_g)/(2\pi c) = 0.01$ ns
τ_{rr}	radiative recombination lifetime	1 ns [19]
τ_{nr}	Nonradiative recombination lifetime	1 ns [19]
τ_c	total carrier recombination lifetime	$\tau_{rr} + \tau_{nr}$

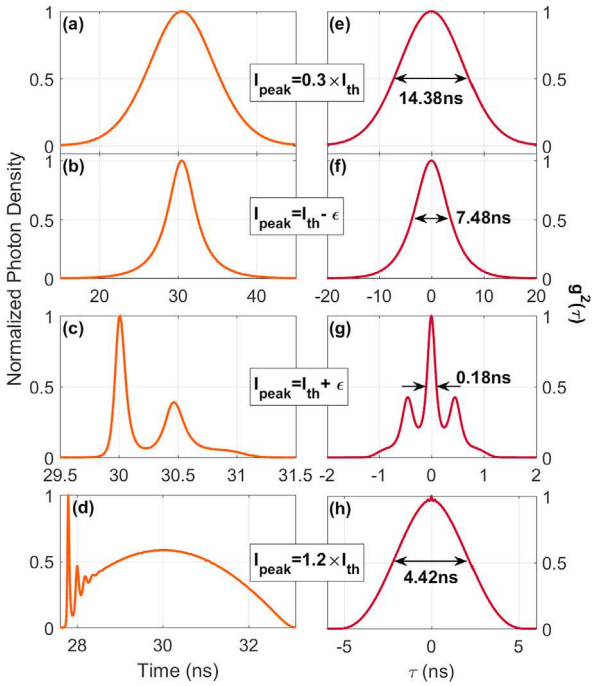

Fig. 3. (a)–(d): Normalized output photon densities (NOPDs) as functions of time generated by numerically solving the rate equations with $\beta = 10^{-5}$ and the peak pump intensities set at (a) far below threshold, (b) slightly below threshold, (c) slightly above threshold and (d) well above threshold. (e)–(h): The simulated $g^2(\tau)$ obtained by taking the autocorrelation of the normalized output photon densities in (a)–(d). The photon densities in (c) and (d) exhibit multiple pulses as a result of relaxation oscillations.

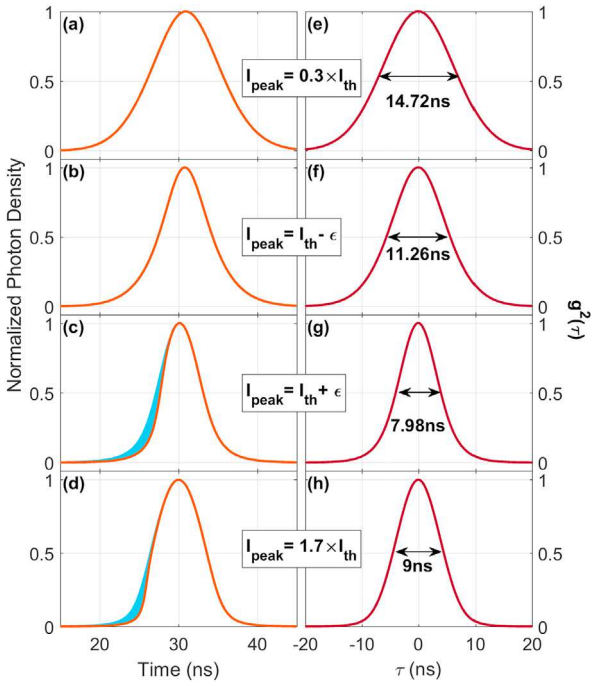

Fig. 4. (a)–(d) NOPDs as functions of time generated by numerically solving the rate equations with unity β (i.e. $\beta = 1$) and the peak pump intensities set at (a) far below threshold, (b) slightly below threshold, (c) slightly above threshold and (d) well above threshold. (e)–(h) The simulated $g^2(\tau)$ obtained by taking the autocorrelation of the NOPDs in (a)–(d). Only single pulses are visible even for the above-threshold NOPDs shown in (c) and (d) because the relaxation oscillation is rapidly damped for a unity-β laser.

(i.e. 10^{-5}) exhibit the same evolutional trends in width as the pump intensity increases from far below to far above threshold.

On the other hand, the minimal $g^2(\tau)$ width of a unity-β nanolaser is approximately 44 times larger than that of a laser with $\beta = 10^{-5}$ as demonstrated in Figs. 3(g) and 4(g). There are two factors that contribute to a shorter $g^2(\tau)$ for a low β nanolaser. Let us first qualitatively examine equation (2), which directly governs the time evolution of the photon density. It is evident that as β approaches zero, the last term involving β becomes orders of magnitude smaller than the first two terms in equation (2) and therefore, can be neglected. Now, without a significant amount of photons contributed by spontaneous emission, the photon decay is expected to be faster, leading to a shorter output photon pulse.

Additionally, Fig. 3(c) clearly shows that two output photon pulses appear for a low β laser while only a single pulse is visible in the case of a unity-β nanolaser [Fig. 4(c)]. The double-pulse effect in the case of a low β laser is a manifestation of relaxation oscillations (ROs) under a time-varying pump. This is a well-known phenomenon for a class-B laser, whose carrier lifetime, τ_c, is longer than the cavity damping time, τ_p. Since we are considering MCPMNL, whose cavity Q is generally on the order of a few thousand in the ideal case, the photon lifetime, τ_p, is estimated to be about 10 ps assuming 1550 nm emission. Hence, such lasers are indeed operating in the class-B regime (see Table 1 for specific values of τ_p and τ_c). Although ROs exist in simulations for both a low-β laser and a unity-β nanolaser, it can be shown that these oscillations are quickly damped for a unity-β nanolaser such that a single pulse output is preserved as shown in Fig. 4(c).

In fact, the higher the β factor is, the faster the RO damping rate is. This can be demonstrated via an analytical analysis. We first consider the frequency response of the photon density fluctuation under a small perturbation in the pump intensity. The general form of the small-signal modulation transfer function (SSMTF) can then be derived by following a standard procedure presented in Ref. 28. Next assuming that the pump variation around threshold can be approximated by a simple unit step function, equation (2) can be solved analytically by taking the inverse Fourier transform (FT) of the product of the SSMTF and the FT of the unit step function. The result is summarized below,

$$\Delta S(t) \propto 1 - \frac{e^{-\omega_n \xi}}{\sqrt{1-\xi^2}} \sin\left(\omega_n \sqrt{1-\xi^2}\, t + \phi_p\right), \tag{4}$$

where $\varphi_p = arctan[(\sqrt{1-}\ \xi 2)/\xi)]$ and $\Delta S(t)$, ω_n and ξ represent the time varying photon density fluctuation, the relaxation oscillation frequency and the damping factor, respectively. Evidently there exists an exponential damping factor, which depends on β [28], in front of the sinusoidal relaxation oscillation term. Equation (4) is plotted in Fig. 5 for three different values of β. As shown, when β is negligible (i.e. $\beta = 0$), several periods of the RO can be observed. The maximum overshoot in the output intensity during the first oscillation period can be as large as 50% of the steady-state intensity when $\beta = 0$. As β increases, both the maximum overshoot and the number of observable oscillation periods decrease due to stronger damping. When β equals to unity, both the overshoot and the oscillation period are insignificantly small. These analytical results agree well with the numerical results shown in Figs. 3(c) and 4(c). Fig. 5 indicates that the relaxation oscillation period is on the order of 100 ps for $\beta = 0$, which also matches the oscillation period shown in Fig. 3(c). Interestingly, careful examination of Fig. 3(c) shows that the period of the second oscillation pulse is longer than that of the first pulse. This is because the pump is modeled as a Gaussian pulse instead of a unit step function in the numerical simulation to match the experimental conditions in Ref. 12. Since both the relaxation oscillation amplitude and frequency are proportional to the pump intensity [28], as the instantaneous pump intensity decreases after the maximum of the Gaussian pump, the second pulse reduces in both amplitude and frequency as expected. RO can also be observed in Fig. 3(d) where the peak pump intensity is much higher than it is in

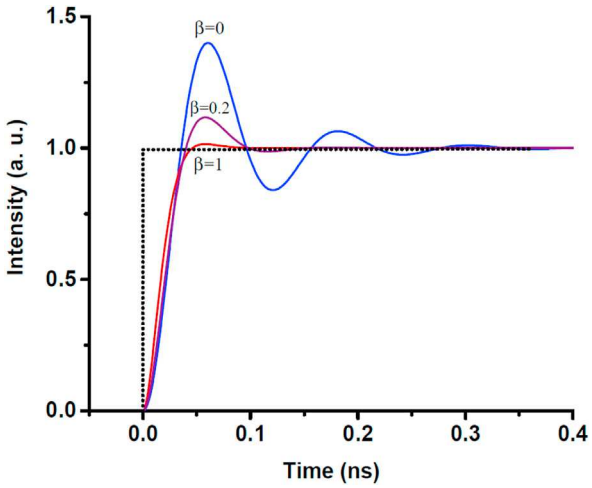

Fig. 5. Simulated responses of lasers (with various β), governed by equations (2) and (3), when subjected to a unit step function perturbation. A laser with negligible β (i.e. $\beta = 0$) exhibits a large overshoot and several relaxation oscillation periods. As β increases, both the overshoot and the number of observable relaxation oscillation periods decrease due to relatively stronger damping. These results obtained analytically agree well with our numerical simulations presented in Figs. 3 and 4 and explain why multiple pulses exist above threshold for a low-β laser while only single pulses are visible for a unity-β laser.

Fig. 3(c); consequently, the RO appears at an earlier time and exhibits a higher frequency.

Due to the multi-pulse behavior in the output photon density, the autocorrelation, $g^2(\tau)$, also naturally exhibits multiple pulses [Fig. 3(g) and (h)]. In this case, the definition of the $g^2(\tau)$ width becomes ambiguous. Instead of calculating the width, we can integrate the total area underneath the $g^2(\tau)$ function and use it as a metric for identifying the SE, ASE and lasing regimes. In Fig. 6, we plot the integrated area of $g^2(\tau)$ as a function of peak pump intensity. Similar to the width variation, the $g^2(\tau)$ area is large far below threshold, decreases with increasing pump intensity below threshold, reaches a minimal slightly above threshold and increases far above threshold. As β increases, the pump intensity corresponding to a minimal $g^2(\tau)$ area decreases, which is consistent with the theoretical expectation that the lasing threshold decreases as β increases [11]. Interestingly, the unity-β curve also exhibits a minimal area, suggesting that there exists a threshold even for a unity-β laser, at least under the nanosecond-pulse pumping condition. This result derived from a purely classical rate-equation model agrees with the theoretical prediction obtained from a comprehensive quantum-optical model discussed previously [30].

3. Direct modulation of nanolasers

Many theoretical analyses [20] [56–58], and studies on response times under femtosecond pump pulses [14] [59], have suggested that nanolasers have potential for high speed modulation. However, few demonstrations of direct modulation have been reported in recent years. The first direct modulation of nanolasers was performed on 2D PhC nanolasers by Altug et al. with a streak camera in 2006 [14]. Besides measuring the response time of their nanolasers to be as small as 2.13 ps, the authors also measured the turn-on delay time to be 1.5 ps in a large signal modulation scheme. Most importantly, a direct modulation measurement with consecutive femtosecond pump pulses separated by 9 ps was conducted where the PhC nanolaser's emission was shown to follow that of the pump. Therefore, Altug et al. experimentally demonstrated the fundamental modulation speed of their 2D PhC nanolasers to be beyond 100 GHz. Nevertheless, the devices measured in this study operated at cryogenic temperatures between 7 K and 150 K, rendering them less suitable for practical applications. The first demonstration of direct optical modulation at room temperature was reported a few years later with a similar type of PhC nanolaser to that of Altug et al. [15]. The PhC nanolaser in Matsuo et al.'s study operated at room temperature under CW optical pumping. The direct optical modulation for this device was conducted in a small signal modulation scheme. The 3-dB direct modulation bandwidth was experimentally measured to be 5.5 GHz with estimated operation energy of as low as 13 fJ per bit. In addition to PhC nanolasers, a nanowire laser placed in a line defect of a 2D PhC lattice was also studied recently [18]. This nanowire laser is capable of operating under CW optical pumping at 4 K. A direct optical modulation measurement with this nanowire laser was conducted with two single photon detectors in an HBT setup. A small signal modulation at 12 GHz and a large signal modulation at 10 Gb/s were demonstrated. Unfortunately, the cryogenic operating temperature of this nanolaser is much too low for it to be implemented in any practical devices.

In addition to room temperature operation, electrical injection and subwavelength physical dimensions are desirable for practical applications. All the devices mentioned above were tested via optical pumping with device footprints ranging from ~10 μm^2 to ~100 μm^2. On the other hand, metal-clad nanolasers can achieve subwavelength footprint in all three physical dimensions [35–47]. While many room-temperature metal-clad nanolasers have been demonstrated in recent years, no direct modulation measurement of any such nanolasers under either optical pumping or electrical injection has been conducted to our knowledge. This is likely due to the higher lasing threshold required for metal-clad nanolasers which often necessitates optical pulse pumping for such devices. On the other hand, CW pumping condition is a prerequisite for direct small-signal modulation such as those conducted in Refs. 15 and 18. Ding et al. have previously demonstrated a room-temperature metallic-cavity nanolaser operating under CW electrical injection [46]. However, the

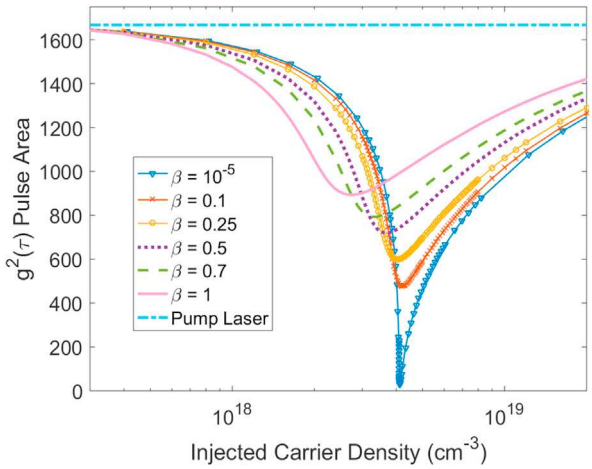

Fig. 6. The integrated areas of the simulated $g^2(\tau)$ pulses such as those shown in Fig. 3(e)–(h) is plotted as a function of the peak pump intensity for different values of β. Also shown is the pump pulse width, which is kept invariant as the maximum pump intensity changes. The minimum pulse area of a laser with $\beta = 10^{-5}$ is 44 times smaller than that of a unity-β laser. Meanwhile, even the pulse area of a unity-β laser exhibits a minimum, suggesting the existence of a threshold, at least under nanosecond pulse pumping.

authors did not perform any direct current modulation measurements.

Here we show the results of the first attempt to directly modulate an electrically pumped metallo-dielectric nanolaser (EPMDNL). We adopted the device design and fabrication detailed in Refs. [47] and [60]. A scanning electron microscope image (SEM) in Fig. 7(a) shows the nanolaser structure after a pedestal, comprising of an InGaAs gain layer and several highly doped InP/InGaAs layers used for current injection, was created via reactive ion etching (RIE) and selective wet chemical etching. Fig. 7(b) displays the same device after aluminum oxide (Al_2O_3) and top electrode (Ti/Pd/Au) depositions. The physical volume of our nano-cavity is estimated to be $V = \pi R^2 h \approx 1.25\lambda^3$, where the radius R, height h and the emission wavelength λ are approximately 900 nm, 1470 nm and 1440 nm, respectively. The lasing characteristics of our device are demonstrated in Fig. 8. At 77 K, the clear kink in the LL-curve [Fig. 8(b) and inset] and the narrow linewidth above threshold [Fig. 8(a) and inset] unambiguously confirm lasing.

The nanolaser was subjected to a small-signal current modulation at 15 MHz, which is the maximum frequency attainable with our current source. The nanolaser emission was directed to two Geiger-mode avalanche photodiode single photon detectors in an HBT configuration. We adopted a similar measurement technique to the one explained in Ref. [18]. The intensity correlation function, $g^2(\tau)$, of the nanolaser emission is shown in Fig. 9(a). Careful examination of Fig. 9(a) suggests the presence of a sinusoidal intensity fluctuation. Indeed, its FT shown in Fig. 9(b) clearly exhibits two distinct peaks – one at 15 MHz and the other at 30 MHz. The small-amplitude peak at 30 MHz arises from the second harmonic in the current source, which we observed via an oscilloscope. Since $g^2(\tau)$ is the autocorrelation of the nanolaser emission, it captures any intensity fluctuation in the nanolaser output. Hence, the modulation frequency observed in $g^2(\tau)$ corresponds exactly to that of the nanolaser emission. Therefore, we have demonstrated that our electrically pumped nanolaser can respond to direct current modulation at 30 MHz.

We further attempted to modulate the nanolaser with a high-speed source operating in the gigahertz regime. However, we could not observe any gigahertz modulation from the nanolaser emission. We believe this is mainly due to high transmission loss in the electrical wires inside the cryostat, which kept our nanolaser at 77 K during experiments. The unshielded CAT4-type copper wires inside this cryogenic chamber are not designed to transmit high-speed signals in the gigahertz regime [61]. Therefore, it is very likely that the high-speed signals were not transmitted to the nanolaser's electrical contacts due to high loss in these wires. This issue can be resolved by using a probing station that is designed to conduct high-speed electrical experiments at cryogenic temperatures. Of course, another option is to develop a room-temperature nanolaser, a project which is currently in progress [62]. With better equipment, such as a cryogenic probing station, and/or a room-temperature device, we believe even higher modulation speeds can be demonstrated with our EPMDNL's in the near future.

4. Coupled nanolasers

Understanding the dynamics of the emission from a single nanolaser, though desirable, is only a stepping stone. For practical purposes such as functioning as on-chip sources for future integrated photonic circuits, multiple such nanoscale lasers will have to be characterized. Once the dynamics of a single emitter can be fully understood, the approach can be adapted and applied to systems containing a multitude of sources. The realization of multiple closely spaced coherent sources, however, would require that the independence of each source is maintained. In other words, operating or modulating one laser should be possible without affecting, in any manner, the emission from its neighbors. The isolation of such densely packed nanolasers is especially imperative for communication, sensing and beam steering applications [63]. Owing to their miniscule footprint, uncoupled nanolasers are especially suited to be packed at high densities compared to macroscale lasers. For example, Qing et al. [63] estimate that about 12,000 photonic-crystal lasers, like the ones used in Ref. [64] with a pitch of 5 μm, would have an equivalent footprint to that of 4 commercially available VCSELs with a pitch of 250 μm between lasers [65].

It has been shown that when two or more cavities are placed in proximity of one another, coupling between the optical modes of the resonators is observed. This phenomenon of coupling has been reported for a variety of resonator architectures such as in photonic molecule microdisk lasers [55] [66–69], photonic-crystal nanocavities [13] [70], and microring lasers [71], [72]. In such coupled

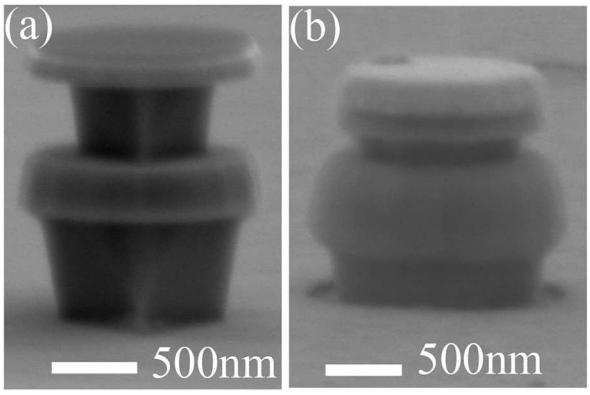

Fig. 7. SEM images of the electrically pumped nanolaser used for direct current modulation show the device after (a) RIE and selective wet chemical etching and (b) conformal Al_2O_3 and top electrode (Ti/Pd/Au) depositions.

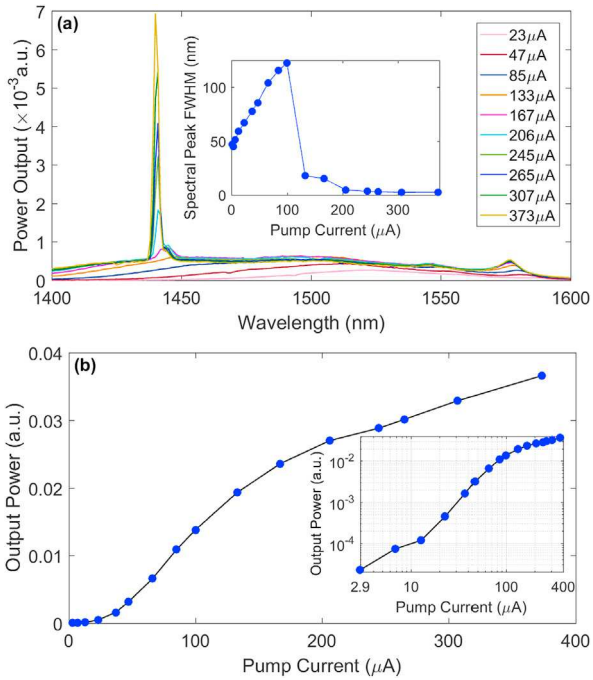

Fig. 8. Lasing demonstration from an EPMDNL. (a) Emission spectra at different pump currents; the lasing peak appears at 1440 nm. The spectral linewidth versus the pump current is plotted in the inset. (b) LL-curve: output power of the EPMDNL versus injected current. The inset shows the same LL-curve data in log-log scale. Lasing action is confirmed by both the linewidth narrowing shown in (a) and the clear kink in the LL-curve in (b).

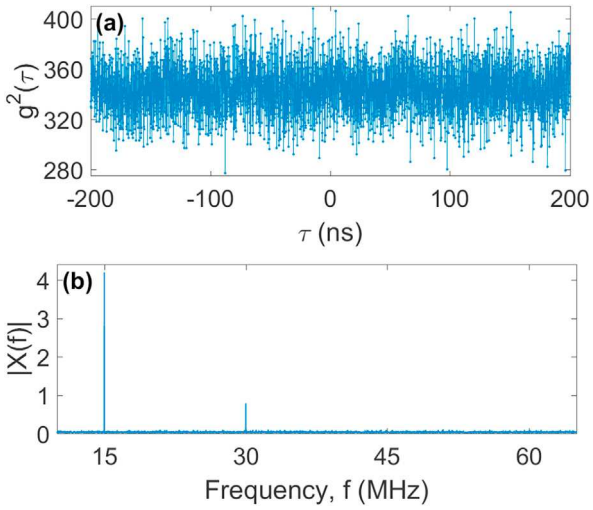

Fig. 9. (a) Experimental $g^2(\tau)$ data and (b) its FT of an EPMDNL under direct current modulation. The FT of the $g^2(\tau)$ shown in (b) clearly demonstrates that the nanolaser emission is sinusoidal with two distinct frequencies at 15 MHz and 30 MHz. High transmission loss in the regular-grade wires inside the cryogenic chamber inhibited high-speed modulation in the gigahertz regime.

systems, an increased evanescent interaction between the electromagnetic fields from each resonator causes a bifurcation in both the frequency and loss of the optical modes [13] [55], [66] [69], [73]. From the standpoint of achieving dense chip-scale integration, coupling is undesirable since it compromises the goal of maintaining independence of the emitters from one another.

Metallo-dielectric nanolasers, such as the ones described in Pan et al. [12] and in Ref. [44], are especially suited to achieve high on-chip packing density. With their truly subwavelength-size in all three dimensions, even greater numbers of these metal-clad nanolasers than photonic-crystal lasers, for example, can be packed in a small area; assuming a diameter of 1.5 μm along with a pitch of 3 μm for a typical metal-clad device, it is possible to place almost 30,000 such nanolasers in the same footprint as 4 commercial VCSELs [63]. Another advantage of metallo-dielectric nanolasers is that, when compared to other implementations of nanolasers where the optical mode spatially spreads beyond the resonator's physical boundaries upon miniaturization, the metal cladding helps to confine

the optical mode inside the gain core while the dielectric shield prevents a high mode-metal overlap, thus reducing losses. Ideally, due to its large metal absorption at the telecom wavelengths these lasers are designed to operate at, the metal in these lasers should also inhibit cross-talk between neighboring nanolasers by preventing the optical modes from interacting.

Recently, a study by Deka et al. analyzed the effects of two metallo-dielectric nanolasers, as shown in Fig. 10, near one another [21]. The objective was to vary the distance between the dielectric shields of the cavities, depicted by d in Fig. 10, to observe if coupling was induced despite the presence of the metal. The gain media were modeled using bulk InGaAsP with each active layer cladded with a thin layer of SiO_2. An airgap designed below the gain provided optimal mode confinement. Finally, a layer of Ag was used to clad the entire system. The values for the permittivities of the material constituents in the model were chosen assuming room temperature operation and considering the wavelength supported by the cavities (around 1.55 μm).

Deka et al. first considered two extreme cases – one where the cavities are placed far apart with $d = 90$ nm and the other where the dielectric shields are in contact with $d = 0$ nm. Plotting the electric field intensity distribution for each distance yielded the side and top mode profiles shown in Fig. 11. When the cavities are designed far apart, it was found that the mode supported by each cavity is independent and isolated from that supported by its neighbor as seen in Fig. 11(a). Since the resonators are identical in size, however, the TE_{011} modes exhibited by the two cavities are at the same resonance frequency and share the same modal profile. The independence of the modes at this value of d is due to the metal between the resonators which damps any evanescent fields arising from each of the gain media, thereby preventing any significant coupling from occurring. In the other extreme case, when $d = 0$ nm, two new optical modes are observed – the anti-bonding and the bonding state – in Fig. 11(b) and (c) respectively. At this intercavity spacing, owing to increased evanescent interaction between the electromagnetic fields, the system supports these two new supermodes as opposed to the independent, isolated cavity modes seen in Fig. 11(a). Additionally, the study revealed that the bonding mode demonstrated a poor confinement of the optical mode to the gain media compared to its anti-bonding counterpart with the mode profile of the latter closely matching that of the independent isolated modes.

To shed further light on the impact of coupling between the two cavities, the study then reported the eigenmode wavelength, λ, and the quality factor, Q, for the modes supported by the system as d was varied in an eigenfrequency solver. As illustrated in Fig. 12(a), for larger values of d, the λs of the two modes are almost equal to one another; a similar observation can be made for the Q of the modes shown in Fig. 12(b). The authors state that this behavior is in line with what is observed in the mode profiles of the magnitude of the electric field for large values of d [Fig. 11(a)]; due to the independent but identical resonances supported at these intercavity spacings, the eigenmode wavelength and loss of the two modes are comparable. As d is reduced further, increased evanescent field interaction between the nanocavities leads to the creation of anti-bonding and bonding supermodes as shown in Fig. 11(b) and (c) respectively. For the bonding mode, the λ and Q are found to be higher and lower, respectively, than the same quantities for an independent, isolated cavity mode like the one in Fig. 11(a). This behavior for the bonding mode is caused by its high overlap with the dissipative metal, which leads to a high loss (low Q) and hence higher λ (since λ is inversely proportional to Q) For the anti-bonding mode, the reverse is true – the λ and Q for this mode are lower and higher than those for an independent, isolated cavity mode. Owing to the contradictory characteristics of these new supermodes, a resultant split in the λ and Q of the modes of the system is shown in the study as seen in Fig. 12(a) and (b) respectively, with the bifurcation easily discernible as d is reduced below 50 nm. The report also describes that the splitting exponentially increases as d is reduced, with the maximum difference in the λ and Q of the bonding and anti-bonding modes observed to be $\Delta\lambda = 14.6$ nm and $\Delta Q = 1347$ at $d = 0$ nm.

With the nanocavities designed to function as lasers, Deka et al. write that quantities such as the wavelength and loss provide no insight into the impact of coupling on lasing tendency. Therefore, they calculate the gain threshold for each mode with the equation:

$$g_{th} = \frac{2\pi n_g}{\lambda Q \Gamma} \tag{5}$$

where n_g is the group refractive index, Γ is the electromagnetic mode confinement factor and λ and Q are the eigenmode wavelength and quality factor for each mode as discussed earlier. With the high loss experienced by the bonding mode, the gain threshold for this mode was found to be much higher than that of the anti-bonding state. The contrast between the g_{th} of the two modes is reported to be as high as $\Delta g_{th} = 217\ \mathrm{cm}^{-1}$ when the resonators are closest (i.e. at $d = 0$ nm).

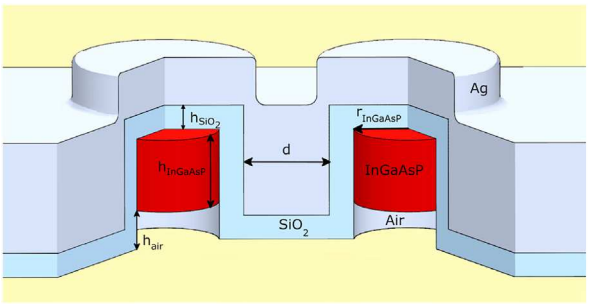

Fig. 10. Schematic of the dual metallo-dielectric cavity system. The heights of the gain, SiO_2 cladding, airgap and the radius of the gain are represented by $h_{InGaAsP}$, h_{SiO2}, h_{Air} and $r_{InGaAsP}$ respectively. The distance, d, between the dielectric shields is varied in an eigenfrequency solver (Reprinted from Ref. [21]).

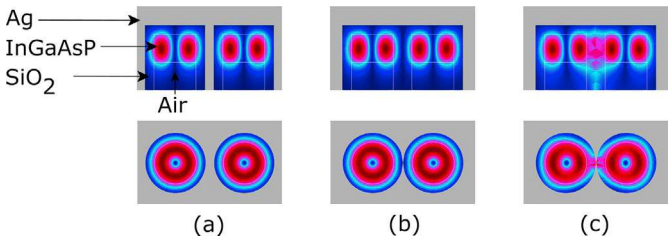

Fig. 11. Electric field intensity profile across side (top row) and top (bottom row) cross-sections of the dual nanolaser system. (a) $d = 90$ nm and two identical but independent modes are supported. (b) $d = 0$ nm and an anti-bonding supermode is created which confines the electromagnetic mode strongly to the gain medium (c) $d = 0$ nm and a new bonding mode is also created but with poor confinement to the active gain regions (Reprinted from Ref. [21]).

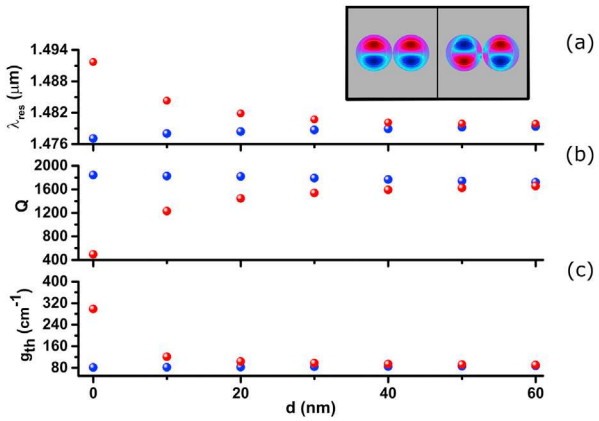

Fig. 12. Eigenmode wavelengths, *Q*-factors and gain thresholds for the two modes of the system vs. *d*. Red represents the bonding state and blue the anti-bonding state at lower values of *d*. (a) The eigenmode wavelength, λ (b) the *Q*-factor and (c) gain threshold, g_{th}. Inset: Electric field distribution of the anti-bonding (left) and bonding (right) supermode. (Reprinted from Ref. [21]). (For interpretation of the references to colour in this figure legend, the reader is referred to the Web version of this article.)

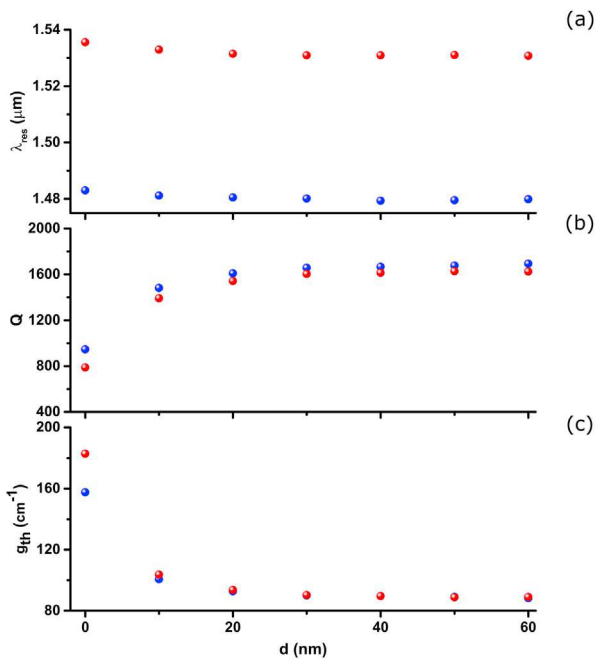

Fig. 13. Resonance wavelengths, *Q*-factors and gain thresholds for the two modes of the system at different *d* like in Fig. 12. The radius of one of the cavities (shown in red) is designed to be five percent larger than that of the other cavity (in blue). (a) The eigenmode wavelength, λ (b) the *Q*-factor and (c) gain threshold, g_{th} (Reprinted from Ref. [21]). (For interpretation of the references to colour in this figure legend, the reader is referred to the Web version of this article.)

4.1. Decoupling by detuning resonances

The finding that coupling is exhibited in closely spaced metallo-dielectric nanolasers despite the presence of metal, as detailed in Ref. [21], hampers progress towards dense integration of such lasers. Coupling means that each individual nanolaser in an array or cluster of nanolasers can no longer be independently operated or modulated, a necessary trait for any practical on-chip source.

In their work, Deka et al. acknowledge the undesirability of coupling for their system since the end goal is to achieve high-packing density and therefore provide a method to inhibit the phenomena from occurring. They report that by slightly detuning the resonance of one cavity relative to the other, the eigenmode wavelengths of the modes can be shifted far enough apart to hinder the onset of any strong coupling. The authors implement this detuning by designing one cavity's radius to be 5% larger than that of its neighbor. Subsequently, the same parameters – λ, Q and g_{th} - as were shown in the study for the case of two identical sized cavities were recalculated for the now size-mismatched cavities. In the results, shown in Fig. 13, no significant splitting in any of the three quantities were observed. The values for $\Delta\lambda$, ΔQ and Δg_{th} at $d = 0$ nm are reported to be 52.5 nm, 157 and 25.15 cm^{-1} respectively. Both the ΔQ and Δg_{th} for the size-mismatched case are much lower than when coupling is pronounced for equal-sized cavities and the increase in $\Delta\lambda$ is only due to the offset in the resonances of the cavities due to the dissimilarity in sizes. Therefore, altering the physical dimensions of one cavity relative to the other provides a way to prevent coupling from occurring and helps preserve the independence of the two nanolasers in the system.

4.2. Decoupling by increasing radius

An alternative method to impede coupling is to design all the resonators in the system to be larger in size. Doing so increases the order of the optical modes supported by the resonators with these higher-order modes better confined to the individual cavities than lower-order ones [74], [75]. As a result, less of the mode leaks out of the gain media even at small intercavity spacing, d, leading to negligible evanescent interaction of the electromagnetic fields and hence decoupling. This technique can be applied to the metallo-dielectric nanolasers presented in Ref. [21]; an example can be seen in Fig. 14 which illustrates the Q-factors of the modes supported by the dual nanolaser system when the radius of each cavity is increased to 275 nm from the original 225 nm studied in the work. Due to the increase in the radii, more than just two modes, as is the case for the smaller-sized cavities shown in Fig. 13, can be observed for the enlarged-cavity system. Additionally, the Q-factors of all the modes except one stay relatively constant or increase slightly as d is reduced. Only one mode exhibits a higher loss (lower Q) with decreasing d. This mode exclusively experiences the increased loss due to coupling (due to a high overlap with the lossy metal) compared to the rest of the modes supported by the system. As the radius of the cavity is further increased, the trend that only one mode of the system demonstrates a low Q as d approaches 0 nm while the remainder of the cavity modes do not experience any significant change in their Q-factors, remains consistent.

Considering only this coupled mode and calculating the difference in its Q - $\Delta Q_{coupled}$ - for when the nanolasers are designed far apart ($d = 100$ nm) and when their shields are in contact ($d = 0$ nm) for different sized cavities yields the plot in Fig. 15. As can be seen in the schematic, with increased radius, the coupled mode exhibits reduced fluctuation in its Q despite the continual decrease in d. Consequently, this mode starts resembling the other modes supported in the system in that it too becomes less susceptible to losses generally experienced due to coupling. In Ref. 74, coupling between micron-sized metal/Si disks is shown to be inhibited via an observed reduction in the difference between the eigenmode wavelengths of anti-bonding and bonding modes as the mode number supported by the disks is increased. Similarly, in the case of the metallo-dielectric nanolasers, the decrease in the loss incurred by the cavity modes, and especially by the one coupled mode in the system, as the cavity radius is increased to support higher-order modes is also indicative of reduced coupling between the cavities. Thus, increasing the physical dimensions of all the constituent resonators of the system provides an additional means of prohibiting coupling for nanolasers which are purposed for compact on-chip integration.

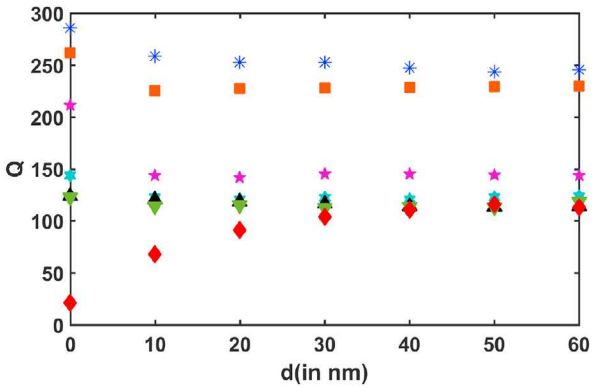

Fig. 14. The Q-factors for the modes supported in a dual nanolaser system with cavity radius = 275 nm for different values of d. Only one of the modes, shown in red, experiences higher losses as d is decreased down to 0 nm; the Q for the rest of the cavity modes either stays constant or increases only slightly. (For interpretation of the references to colour in this figure legend, the reader is referred to the Web version of this article.)

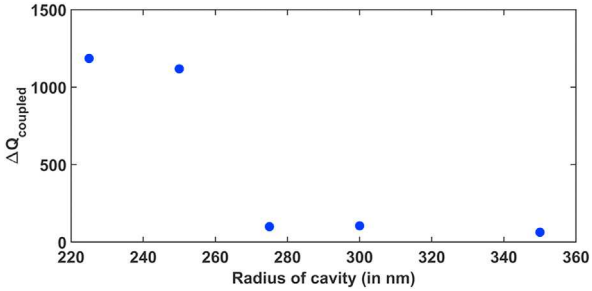

Fig. 15. Difference in *Q*-factor for the coupled mode - $\Delta Q_{coupled}$ – for $d = 100$ nm and $d = 0$ nm for varying radii of the cavities. As radius is increased, there is less loss experienced by the mode as d is reduced since coupling becomes less pronounced.

5. Discussion and future perspectives

5.1. Integration with silicon photonics

Despite the recent progress presented in the previous sections of this article, several major areas of development are still needed before practical applications can be realized. One of the greatest challenges of integrating nanolasers onto a densely packed photonic integrated circuit (PIC) is to efficiently couple the nanolasers' output to silicon waveguides such that the information encoded in the optical signal can be transferred to other parts of the photonic chip with minimal loss. More importantly, the entire fabrication process of both the nano-cavity and waveguide should be CMOS compatible. Recently, a group of researchers in France demonstrated the first room-temperature, CW electrically pumped 1D PhC nanolaser efficiently coupled to a silicon waveguide [76]. The authors employed a high-yield wafer-bonding technique to achieve heterogeneous integration of InGaAsP, which comprises the active core of the nanolaser, onto a silicon wafer with pre-fabricated waveguides. The PhC nanolaser is subsequently fabricated with a top-down approach which bypasses any CMOS incompatible fabrication steps. The fabricated device demonstrated a record high wall-plug efficiency of 14%. However, the threshold current of this nanolaser was reported to be 100 μA, 20 times higher than the best electrically pumped PhC nanolasers demonstrated under CW operation at room temperature [77], although the latter devices were not coupled to any waveguide. The authors of Ref. 76 speculated that the threshold current can be reduced by lowering the cavity-to-waveguide coupling strength and reducing the volume of the active region.

In addition to reducing the threshold current, it is also desirable to further reduce the device footprint. As discussed in section 2 of this article, despite the excellent performance of PhC nanolasers, at least one physical dimension exceeds ten microns due to the many lattice periods necessary to achieve tight optical confinement. On the other hand, MCPMNL [12] [43–47], can achieve sub-wavelength footprints in all three physical dimensions while still maintaining reasonably low loss at telecom wavelengths. While room-temperature CW electrically pumped MCPMNL have been demonstrated [46], research on coupling this type of nanolaser to silicon waveguides is lacking mainly due to fabrication challenges. As nanofabrication techniques mature overtime, however, this yet unexplored research path may become feasible soon.

5.2. Tunable nanolasers

Another research subject undergoing intense study in recent years focuses on the development of tunable nanolasers. For on-chip optical communication and signal processing, integrated tunable laser sources are often desirable due to their applicability in wavelength division multiplexing, which enhances the communication bandwidth and enables bidirectional communication. Recently, a tunable nanolaser based on Raman scattering was reported by Zhu et al. [78]. These authors employed a novel material, a freestanding ZnO-graphene superlattice, grown via a spatially confined reaction method. Since the energy of Raman scattered photons depends on the energy of the incident photon, the lasing wavelength can be modified by simply changing the pump laser wavelength. Specifically, the device in Zhu et al.'s article was coherently pumped at 488 nm, 514.5 nm, 568 nm, 647 nm and 785 nm. For each pump laser wavelength, four Raman scattered emission peaks appeared in the spectra centering on 505 nm, 532.5 nm, 590 nm, 675 nm and 830 nm, respectively. Therefore, the total tuning range was found to be roughly from 490 nm to 860 nm. While the tuning range was very wide, only discrete tuning was demonstrated since the nanolaser depends on coherent pumping from an argon-krypton ion laser, which emits discrete spectral lines itself.

In contrast to the Raman scattering nanolaser, the plasmonic laser developed by Yang et al. can be tuned more continuously in the spectral domain [79]. This tunable laser is based on a gold nano-particle array with dye molecules dissolved in liquids of variable refractive indices serving as the gain media. Tuning of the lasing emission was achieved by varying the refractive index of the environment around the gold nano-particles by simply changing the liquid solvents used for the gain medium. Since the refractive indices can be finely tuned by mixing different solvents, the laser emission can also be altered with a higher degree of precision than that of the Raman scattering nanolaser. Although the demonstrated tuning range was as wide as 50 nm, due to the intrinsic emission properties of the dye molecules employed as the gain medium, the emission wavelength was limited to between 850 nm and 900 nm – far from the

telecommunication bands. Additionally, due to the liquid gain medium, it is difficult to integrate such a laser with other on-chip passive components based on silicon photonics.

Instead, tunable PhC and metal-clad nanolasers based on solid inorganic III-V gain media are more realistic candidates for chip-scale communication and signal processing. Several tunable nanolasers based on 1D [80] [81], and 2D PhC lattices [82] [83], embedded in a stretchable material, polydimethylsiloxane (PDMS), have been demonstrated in recent years. Based on an InGaAsP gain medium, these devices operate in the telecom wavelength range. Tuning is achieved by compressing and stretching the PDMS substrate, which changes the resonance of the PhC lattices. The widest tuning range was reported by Lu et al. to be 155 nm (from 1452 nm to 1608 nm), covering almost the entire S + C + L bands [81].

While the wide-range tuning with a flexible carrier substrate such as PDMS is promising, the proof-of-concept demonstrations described in the previous paragraph are achieved by manually stretching and compressing the substrate with a mechanical stage. A more practical approach would be to develop a method to control the mechanical motion electrically. It will be even more promising if the electronic control can be integrated onto the same chip. One possible technique is to employ microelectromechanical systems (MEMS). While tuning of passive PhC cavities with MEMS has already been demonstrated [84], the same approach has not been explored for tuning active PhC nanolasers. Moreover, we are unaware of any tunable metal-clad nanolasers that have been demonstrated. These are open research areas that have yet to be explored.

5.3. Dynamics of coupled nanolasers

Finally, while coupling between neighboring nanolasers is undesirable when independent operation of each laser on a densely packed chip is required, it can be advantageous under other circumstances. For instance, Marconi et al. demonstrated that the high-frequency bonding (B) mode and the low-frequency antibonding (AB) mode in two strongly coupled PhC nanolasers can be engineered such that the B mode has a lower threshold than the AB mode [22]. In this case, mode switching was observed by simply sweeping the pump intensity from low to high. Therefore, tuning of the lasing frequency can be achieved by simply changing the pump intensity. In another article, the same authors showed that super-thermal emission with normalized intensity correlation as high as 3.5 [i.e. $g^2(\tau) = 3.5$] can be engineered in their strongly coupled dual PhC nanolasers [23]. The strongly correlated photons emitted from this coupled system may find applications in areas where multiphoton generation is desirable such as in time-domain ghost imaging.

In a coupled system similar to that of Marconi et al., Hamel et al. demonstrated spontaneous mirror-symmetry breaking (SSB) in PhC nanolasers for the first time [13]. The anti-bonding mode in this coupled system can be tailored such that most of the photons are localized in either one of the nano-cavities such that the L1R0 state represents the left cavity possessing a higher intensity than the right cavity (i.e. $I_{left} > I_{right}$), and the L0R1 state represents the opposite (i.e. I_{left} I_{righ}). Furthermore, the localized photons of one cavity can spontaneously tunnel to the neighboring cavity, leading to a switch in the intensity of the two nanolasers. Hence, spontaneous switching between the L1R0 and the L0R1 state can be achieved. These authors further show that the L1R0 and L0R1 state can be deterministically trigged and stabilized by shining a 100 ps pulsed laser on the right and left cavity, respectively. These characteristics parallel those of an electronic flip-flop. Therefore, this coupled nanolaser system represents an excellent candidate for nanoscale all-optical flip-flops, which can serve as reliable memory elements in PICs.

Future work in this area could involve pursuing similar studies in the quantum regime. For example, the number of photons at the onset of SSB in Ref. 13 is on the order of a hundred. If the threshold of these PhC nanolasers can be reduced such that only ~10 photons are required for SSB to occur, this coupled PhC nanolaser system may become an excellent platform to study quantum correlation between two nonlinearly coupled nano-cavities. Another area of interest is to study similar phenomena in metal-clad nanolasers, especially since Deka et al. have demonstrated that evanescent coupling between two closely spaced metal-clad nanolasers does exist despite their metal coating. Besides the benefit of having smaller footprints, metal-clad nanolasers possess other attractive features such unity-β lasing [37] [45], and high Purcell factors due to smaller mode volumes achievable by using metal. These unique attributes of metal-clad nanolasers may lead to unexpected dynamical behaviors on a faster time scale. It is therefore, another exciting research area waiting to be explored.

5.4. Summary

In summary, we have reviewed state-of-the-art progresses in three important aspects of nanolaser research and development. First, second-order intensity correlation, $g^2(\tau)$, is one of the most reliable techniques to characterize coherence and threshold properties of high-β nanolasers. While most previous publications focused on observing the photon bunching peak at $g^2(0)$ and relying on its suppression to signify the onset of lasing, we showed that the integrated area of an individual $g^2(\tau)$ pulse can also be exploited as an independent parameter to define the SE, ASE and lasing regimes of a high-β nanolaser under nanosecond pulse pumping. With in-depth analysis of the laser rate equations, we showed that the $g^2(\tau)$ pulse area varies in similar fashion for both low- and high-β lasers. However, the minimal pulse area, which occurs at around the lasing threshold, for a high-β nanolaser is much larger than that of a low-β laser. In fact, a low-β class-B laser emits multiple pulses slightly above threshold with the integrated area of the first pulse approaching zero. We invoked an analytical model involving a transfer function technique to explain that the multi-pulse effect of a low-β class-B laser is due to a slowly damped relaxation oscillation. Our analytical model further demonstrated that the relaxation oscillation damping rate increases as β increases.

Secondly, in section 3, we reviewed the cutting-edge demonstrations of direct modulation of nanolasers. While most recent demonstrations employed optical pumping, we demonstrated for the first time direct current modulation of an electrically pumped metallo-dielectric nanolaser at a modulation frequency of 30 MHz. In section 4, we presented the third important aspect concerning nanolaser

research – dense integration – by reviewing two methods of decoupling neighboring metal-clad nanolasers, a practical and imperative aspect towards achieving dense on-chip integration. By increasing the radius of one of the nanolasers by as small as 5% relative to its neighbor, detuning in their emission frequencies can be achieved, leading to effective decoupling between the two nanolasers. Additionally, decoupling is also possible by increasing the radii of the nanolasers slightly such that while their sub-wavelength physical dimensions are preserved, the optical modes are better confined inside the individual nano-resonators.

Lastly, we identified several areas that current nanolaser research is gravitating towards, including integration with silicon photonics, tunable nanolasers and investigation of the dynamics of two coupled nanolasers. We reviewed the cutting-edge results in each area and offered perspectives on future directions.

Funding

This work was supported in part by the National Science Foundation, the Office of Naval Research (ONR), the Army Research Office (ARO), DARPA, the Seminconductor Research Corporation, the Cymer Corporation and the San Diego Nanotechnology Infrastructure (SDNI) supported by the NSF National Nanotechnology Coordinated Infrastructure (grant ECCS-1542,148). S. H. Pan is a recipient of the NSF Graduate Research Fellowship under Grant DGE-1144086.

References

[1] D.A.B. Miller, Are optical transistors the logical next step? Nat. Photon. 4 (Jan. 2010) 3–5.
[2] G. Shambat, et al., Single-cell photonic nanocavity probes, Nano Lett. 13 (Feb. 2013) 4999–5005.
[3] M. Lončar, A. Scherer, Y. Qiu, Photonic crystal laser sources for chemical detection, Appl. Phys. Lett. 82 (Jun. 2003) 4648–4650.
[4] D. Takahashi, et al., Detection of endotoxin using a photonic crystal nanolaser, Appl. Phys. Lett. 106 (13) (Apr. 2015), 131112.
[5] T. Watanabe, et al., Ion-sensitive photonic-crystal nanolaser sensors, Optic Express 25 (20) (Oct. 2017) 24469–24479.
[6] Y. Nakayama, et al., Tunable nanowire nonlinear optical probe, Nature 447 (Jun. 2007) 1098–1101.
[7] A. Kolodny, Energy efficient system architectures, in: Green Photonics and ElectronicsSpringer, Cham, Switzerland, 2017, pp. 203–204 ch. 8, sec. 8.1.
[8] P. Delforge, America's Data Centers Are Wasting Huge Amounts of Energy, Natural Resources Defense Council, New York, New York, U.S.A, Aug. 2014 [Online]. Available: https://www.nrdc.org/sites/default/files/data-center-efficiency-assessment-IB.pdf.
[9] P. Delforge, Data center Efficiency Assessment, Natural Resources Defense Council, New York, New York, U.S.A, Aug. 2014 [Online]. Available: https://www.nrdc.org/sites/default/files/data-center-efficiency-assessment-IP.pdf.
[10] Report to Congress on Server and Data Center Energy Efficiency Public Law 109-431, U.S. Environmental Protection Agency ENERGY STAR Program, Aug. 2, 2007 [Online]. Available, https://www.energystar.gov/ia/partners/prod_development/downloads/EPA_Datacenter_Report_Congress_Final1.pdf?2abe-a80f.
[11] S. Noda, Seeking the ultimate nanolaser, Science 314 (Oct. 2006) 260–261.
[12] S.H. Pan, et al., Dynamic hysteresis in a coherent high-β nanolaser, Optica 3 (11) (Oct. 2016) 1260–1265.
[13] P. Hamel, et al., Spontaneous mirror-symmetry breaking in coupled photonic-crystal nanolasers, Nat. Photon. 9 (Apr. 2015) 311–315.
[14] H. Altug, D. Englund, J. Vuckovic, Ultrafast photonic crystal nanocavity laser, Nat. Phys. 2 (Jul. 2006) 484–488.
[15] S. Matsuo, et al., High-speed ultracompact buried heterostructure photonic-crystal laser with 13 fJ of energy consumed per bit transmitted, Nat. Photon. 4 (Sept. 2010) 648–654.
[16] G. Shambat, et al., Ultrafast direct modulation of a single-mode photonic crystal nanocavity light-emitting diode, Nat. Commun. 2 (Nov. 2011), 539.
[17] R. Ma, et al., Multiplexed and electrically modulated plasmon laser circuit, Nano Lett. 12 (10) (Sept. 2012) 5396–5402.
[18] M. Takiguchi, et al., Continuous-wave operation and 10-Gb/s direct modulation of InAsP/InP subwavelength nanowire laser on silicon photonic crystal, APL Photonics 2 (4) (Apr. 2017), 046106.
[19] E.K. Lau, et al., Enhanced modulation bandwidth of nanocavity light emitting devices, Optic Express 17 (10) (Apr. 2009) 7790–7799.
[20] T. Suhr, et al., Modulation response of nanoLEDs and nanolasers exploiting Purcell enhanced spontaneous emission, Optic Express 18 (11) (May 2010) 11230–11241.
[21] S.S. Deka, et al., Coupling in a dual metallo-dielectric nanolaser system, Opt. Lett. 42 (22) (Nov. 2017) 4760–4763.
[22] M. Marconi, et al., Asymmetric mode scattering in strongly coupled photonic crystal nanolasers, Opt. Lett. 41 (24) (Dec. 2016) 5628–5631.
[23] M. Marconi, et al., Far-from-Equilibrium route to superthermal light in bimodal nanolasers, Phys. Rev. X 8 (1) (Jan. 2018), 011013.
[24] F. Jahnke, et al., Giant photon bunching, superradiant pulse emission and excitation trapping in quantum-dot nanolasers, Nat. Commun. 7 (May 2016), 11540.
[25] D.T. Cassidy, et al., Spontaneous-emission factor of semiconductor diode lasers, J. Opt. Soc. Am. B 8 (4) (Apr. 1991) 747–752.
[26] E.M. Purcell, Spontaneous emission probabilities at radio frequencies, Phys. Rev. 69 (1946), 681.
[27] J.M. Gerard, B. Gayral, Strong Purcell effect for InAs quantum boxes in three-dimensional solid-state microcavities, J. Lightwave Technol. 17 (11) (Nov. 1999) 2089–2095.
[28] L.A. Coldren, S.W. Corzine, Dynamic effects, in: Diode Lasers and Photonic Integrated Circuits, second ed., John Wiley & Sons, inc., New York, New York, 1995, pp. 247–333.
[29] R. Loudon, Classical theory of optical fluctuations and coherence, in: The Quantum Theory of Light, third ed., Oxford Univ. Press, New York, New York, U.S.A, 2000, pp. 82–124 ch. 3.
[30] W.W. Chow, F. Jahnke, C. Gies, Emission properties of nanolasers during the transition to lasing, Light Sci. Appl. 3 (Aug. 2014) e201.
[31] S. Strauf, et al., Self-tuned qunatum dot gain in photonic crystal lasers, Phys. Rev. Lett. 96 (12) (Mar. 2006), 127404.
[32] Y.-S. Choi, et al., Evolution of the onset of coherence in a family of photonic crystal nanolasers, Appl. Phys. Lett. 91 (Jul. 2007), 031108.
[33] R. Hostein, et al., Demonstration of coherent emission from high-β photonic crystal nanolasers at room temperature, Opt. Lett. 35 (8) (Apr. 2010) 1154–1156.
[34] I. Prieto, et al., Near thresholdless laser operation at room temperature, Optica 2 (1) (Jan. 2015) 66–69.
[35] M.A. Noginov, et al., Demonstration of a spaser-based nanolaser, Nature 460 (Aug. 2009) 1110–1112.
[36] D.J. Bergman, M.I. Stockman, Surface plasmon amplification by stimulated emission of radiation: quantum generation of coherent surface plasmons in nanosystems, Phys. Rev. Lett. 90 (Jan. 2003), 027402.
[37] R.F. Oulton, et al., Plasmon lasers at deep subwavelength scale, Nature 461 (Aug. 2009) 629–632.
[38] R. Ma, R.F. Oulton, V.J. Sorger, G. Bartal, X. Zhang, Room-temperature sub-diffraction-limited plasmon laser by total internal reflection, Nat. Mater. 10 (Dec. 2010) 110–113.
[39] R.-M. Ma, R.F. Oulton, V.J. Sorger, X. Zhang, Plasmon lasers: coherent light source at molecular scales, Laser Photon. Rev. 7 (1) (Jan. 2013) 1–21.
[40] Y.-J. Lu, et al., Plasmonic nanolaser using epitaxially grown silver film, Science 337 (6093) (Jul. 2012) 450–453.
[41] S.-H. Kwon, et al., Subwavelength plasmonic lasing from a semiconductor nanodisk with silver nanopan cavity, Nano Lett. 10 (9) (Aug. 2010) 3679–3683.
[42] R. Perahia, T.P. Mayer Alegre, A.H. Safavi-Naeini, O. Painter, Surface-plasmon mode hybridization in subwavelength microdisk lasers, Appl. Phys. Lett. 95 (20) (Nov. 2009), 201114.

[43] M.T. Hill, et al., Lasing in metallic-coated nanocavities, Nat. Photon. 1 (Sept. 2007) 589–594.
[44] M.P. Nezhad, et al., Room-temperature subwavelength metallo-dielectric lasers, Nat. Photon. 4 (Apr. 2010) 395–399.
[45] M. Khajavikhan, et al., Thresholdless nanoscale coaxial lasers, Nature 482 (Feb. 2012) 204–207.
[46] K. Ding, et al., Record performance of electrical injection subwavelength metallic-cavity semiconductor lasers at room temperature, Optic Express 21 (4) (Feb. 2013) 4728–4733.
[47] J.H. Lee, et al., Electrically pumped sub-wavelength metallo- dielectric pedestal pillar lasers, Optic Express 19 (22) (Oct. 2011) 21524–21531.
[48] W. Hayenga, et al., Second-order coherence properties of metallic nanolasers, Optica 3 (11) (Oct. 2016) 1187–1193.
[49] T. Erneux, P. Glorieux, Slow passage, in: Laser Dynamics, Cambridge Univ. Press, New York, New York, U.S.A, 2010, pp. 155–171.
[50] J.R. Tredicce, et al., Critical slowing down at a bifurcation, Am. J. Phys. 72 (6) (Jun. 2004) 799–809.
[51] W. Scharpf, et al., Experimental observation of a delayed bifurcation at the threshold of an argon laser, Optic Commun. 63 (5) (Sept. 1987) 344–348.
[52] F.T. Arecchi, W. Gadomski, R. Meucci, J.A. Roversi, Delayed bifurcation at the threshold of a swept gain CO_2 laser, Optic Commun. 70 (2) (Feb. 1989) 155–160.
[53] A. El Amili, G. Gredat, M. Alouini, I. Sagnes, F. Bretenaker, Experimental study of the delayed threshold phenomenon in a class-A VECSEL, Eur. Phys. J. Appl. Phys. 58 (1) (Apr. 2012), 10501.
[54] C.Y.J. Chu, H. Ghafouri-Shiraz, Analysis of gain and saturation characteristics of a semiconductor laser optical amplifier using transfer matrices, J. Lightwave Technol. 12 (8) (Aug. 1994).
[55] S. Ishii, A. Nakagawa, T. Baba, Modal characteristics and bistability in twin microdisk photonic molecule lasers, IEEE J. Sel. Top. Quant. Electron. 12 (1) (Feb. 2006) 71–77.
[56] K. Ding, J.O. Diaz, D. Bimberg, C.Z. Ning, Modulation bandwidth and energy efficiency of metallic cavity semiconductor nanolasers with inclusion of noise effects, Laser Photon. Rev. 9 (5) (Jul. 2015) 488–497.
[57] C.A. Ni, S.L. Chuang, Theory of high-speed nanolasers and nanoLEDs, Optic Express 20 (15) (Jul. 2012) 16450–16470.
[58] M.I. Stockman, The spaser as a nanoscale quantum generator and ultrafast amplifier, J. Optic. 12 (2) (Jan. 2010), 024004.
[59] R. Röder, et al., Ultrafast dynamics of lasing semiconductor nanowires, Nano Lett. 15 (7) (Jun. 2015) 4637–4643.
[60] Q. Gu, et al., Amorphous Al2O3 shield for thermal management in electrically pumped metallo-dielectric nanolasers, IEEE J. Quant. Electron. 50 (7) (Jul. 2014) 499–509.
[61] CCNA, Network media types, in: CCNA Self-study: CCNA Basics, Cisco System Inc., Cisco Press, 2002 [online]. Available: http://www.ciscopress.com/articles/article.asp?p=31276.
[62] C. Fang, F. Vallini, A. El Amili, J. S. T. Smalley, and Y. Fainman, "Low resistance tunnel junctions for efficient electrically pumped nanolasers," IEEE J. Sel. Top. Quant. Electron., vol. 23, no. 6, Nov.–Dec. 2017, Art. no. 1500506.
[63] Q. Gu, et al., Subwavelength semiconductor lasers for dense chip-scale integration, Adv. Optic Photon 6 (1) (Mar. 2014) 1–56.
[64] H. Abe, M. Narimatsu, S. Kita, A. Tomitaka, Y. Takemura, T. Baba, Live cell imaging using photonic crystal nanolaser array, in: Mirco-tas, 2011, pp. 1433–1435. Seattle, Washington, U.S.A.
[65] Oclaro, Data sheet: 850 nm 20 Gb/s multimode VCSEL chip array [online]. Available: http://www.oclaro.com/datasheets/D00473-PB%20APA7601xy0000%20Datasheet%20Iss01.pdf.
[66] A. Nakagawa, S. Ishii, T. Baba, Photonic molecule laser composed of GaInAsP microdisks, Appl. Phys. Lett. 86 (4) (Jan. 2005), 041112.
[67] S.V. Boriskina, Spectrally engineered photonic molecules as optical sensors with enhanced sensitivity: a proposal and numerical analysis, J. Opt. Soc. Am. B 23 (8) (Aug. 2006) 1565–1573.
[68] S.V. Boriskina, Coupling of whispering-gallery modes in size-mismatched microdisk photonic molecules, Opt. Lett. 32 (11) (Jun. 2007) 1557–1559.
[69] E.I. Smotrova, A.I. Nosich, T.M. Benson, P. Sewell, Optical coupling of whispering-gallery modes of two identical microdisks and its effect on photonic molecule lasing, IEEE J. Sel. Top. Quant. Electron. 12 (1) (Feb. 2006) 78–85.
[70] D. O'Brien, et al., Coupled photonic crystal heterostructure nanocavities, Optic Express 15 (3) (Feb. 2007) 1228–1233.
[71] M.T. Hill, et al., A fast low-power optical memory based on coupled micro-ring lasers, Nature 432 (Nov. 2004) 206–209.
[72] H. Hodaei, et al., Parity-time-symmetric coupled microring lasers operating around an exceptional point, Opt. Lett. 40 (21) (Nov. 2015) 4955–4958.
[73] K.A. Atlasov, K.F. Karlsson, A. Rudra, B. Dwir, E. Kapon, Wavelength and loss splitting in directly coupled photonic-crystal defect microcavities, Optic Express 16 (20) (Sept. 2008) 16255–16264.
[74] Q. Wang, et al., Hybrid photonic-plasmonic molecule based on metal/Si disks, Optic Express 21 (9) (May 2013) 11037–11047.
[75] E.I. Smotrova, A.I. Nosich, Threshold reduction in a cyclic photonic molecule laser composed of identical microdisks with whispering-gallery modes, Opt. Lett. 31 (7) (Apr. 2006) 921–923.
[76] G. Crosnier, et al., Hybrid indium phosphide-on-silicon nanolaser diode, Nat. Photon. 11 (Apr. 2017) 297–300.
[77] K. Takeda, et al., Few-fJ/bit data transmissions using directly modulated lambda-scale embedded active region photonic-crystal lasers, Nat. Photon. 7 (May 2013) 569–575.
[78] H. Zhu, et al., A thresholdless tunable Raman nanolaser using a ZnO–graphene superlattice, Adv. Mater. 29 (2) (Jan. 2017), 1604351.
[79] A. Yang, et al., Real-time tunable lasing from plasmonic nanocavity arrays, Nat. Commun. 6 (Apr. 2015), 6939.
[80] T.W. Lu, C. Wang, C.F. Hsiao, P.T. Lee, Tunable nanoblock lasers and stretching sensors, Nanoscale 8 (Aug. 2016) 16769–16775.
[81] T.W. Lu, C. Wu, C. Wang, P.T. Lee, Compressible 1D photonic crystal nanolasers with wide wavelength tuning, Opt. Lett. 42 (12) (Jun. 2017) 2267–2270.
[82] J.-H. Choi, et al., A high-resolution strain-gauge nanolaser, Nat. Commun. 7 (May 2016), 11569.
[83] M.-H. Shih, et al., Compact tunable laser with InGaAsP photonic crystal nanorods for C-band communication, IEEE J. Sel. Top. Quant. Electron. 21 (6) (Jun. 2015), 4900505.
[84] X. Chew, et al., Dynamic tuning of an optical resonator through MEMS-driven coupled photonic crystal nanocavities, Opt. Lett. 35 (15) (Aug. 2010) 2517–2519.

Si Hui Pan received her B.S. degree in physics in 2010 from Brandeis University, Waltham, MA, USA, and her M.S. degree in physics in 2013 from University of California at San Diego, La Jolla, CA, USA, where she is currently pursuing a Ph.D. in physics. Her research interests include the fabrication and characterization of nanophotonic devices, solid-state physics and quantum optics. Specifically, she is investigating the coherent and dynamical properties of metal-clad nanolasers based on InGaAsP multiple quantum wells. Prior to graduate school, she held a research staff position for two years at the Massachusetts Institute of Technology Lincoln Laboratory, Lexington, MA, USA, where she participated in the research and development of superconducting nanowire single photon detectors. She has held undergraduate research positions at the Daghlian Ion Accelerator Lab at Connecticut College, the Laboratory for Elementary Particle Physics of Cornell University and the National Nanotechnology Infrastructure Network of Harvard University, where she investigated the optical properties of silicon super-saturated with chalcogens for her undergraduate honors thesis. Upon receiving her B.S. degree, Ms. Pan was awarded a research internship position at the National Institute for Material Science, Tsukuba, Ibaraki, Japan. Ms. Pan is a recipient of the National Science Foundation Graduate Research Fellowship, the Physics Excellence Award from University of California at San Diego and the Physics Faculty Prize from Brandeis University.

Suruj S. Deka received both a B.E degree (with *magna cum laude* distinction) and an M.S degree in electrical engineering from Vanderbilt University in Nashville, Tennessee in 2015 as part of an accelerated 4-year-dual-degree program. He is currently a graduate student at the University of California in San Diego pursuing his PhD in electrical engineering in the discipline of nanoscale devices and systems. His main research interest concerns modeling, fabrication and characterization of III-V nanolaser devices. His master's thesis at Vanderbilt University was entitled "*Memristance Phenomenon in TiO_2-Porous Silicon Nanocomposites*" and involved material and electrical characterization of memristive devices. Mr. Deka is the recipient of the Jacobs Fellowship (2015–2016) and the Sandstrom Fellowship (2016–2017).

Abdelkrim El Amili received his B.Sc. in Physics and Engineering from University of Bordeaux 1, Talence, France in 2004, his M.Sc. in Fundamental Physics from the same university in 2006, and his Ph.D. in Physics from University of Paris-Sud XI, Orsay, France in 2010. His thesis work was on the realization of an experimental setup for atom detection in atom-chips, and on the theoretical investigation of detection performances of coupled micro-cavities. From 2010 to 2011 he worked as a postdoctoral researcher in Laser Physics at the Laboratoire Aimé Cotton in Paris, and from 2011 through 2014 he worked as a non-permanent researcher at the Institut de Physique de Rennes 1, CNRS-University of Rennes 1. His research was on the experimental and theoretical study of the dynamics of solid-state lasers. Particularly, he focused on the development of optical methods enabling strong suppressions of inherent resonant intensity noises in single-/dual-frequency solid-state lasers. In 2015, Dr. El Amili joined the ECE department at UC San Diego where he is working as a research scientist. His research interests lie in both III-V and Silicon nanophotonics.

Qing Gu is an Assistant Professor of Electrical and Computer Engineering at UT Dallas since 2016, directing research in the Nanophotonics Lab. She received the Bachelor degree from the University of British Columbia, Canada in 2008, and the Ph.D. degree from the University of California, San Diego in 2014, both in Electrical Engineering. Her research interests include the design, fabrication and characterization of nano- and micro-scale photonic devices (such as lasers, waveguides and sensors), novel light-emitting materials and optical cavity configuration, quantum behavior analysis in nanostructures, and integrated photonic circuits. She is the author of book "Semiconductor Nanolasers" by Cambridge University Press, published in 2017.

Yeshaiahu (Shaya) Fainman is an inaugural Cymer Chair Professor of Advanced Optical Technologies and Distinguished Professor in Electrical and Computer Engineering (ECE) at the University of California, San Diego (UCSD). He received M. Sc and Ph. D degrees from Technion in 1979 and 1983, respectively. He is directing research of the Ultrafast and Nanoscale Optics group at UCSD and made significant contributions to near field optical phenomena, inhomogeneous and meta-materials, nanophotonics and plasmonics, and non-conventional imaging. His current research interests are in near field optical science and technology with applications to information technologies and biomedical sensing. He contributed over 280 manuscripts in peer review journals and over 450 conference presentations and conference proceedings. He is a Fellow of the Optical Society of America, Fellow of the Institute of Electrical and Electronics Engineers, Fellow of the Society of Photo-Optical Instrumentation Engineers, and a recipient of the Miriam and Aharon Gutvirt Prize, Lady Davis Fellowship, Brown Award, Gabor Award, Emmett N. Leith Medal and Joseph Fraunhofer Award/Robert M. Burley Prize.